AIAA JOURNAL
Vol. 34, No. 1, January 1996

Experimental and Numerical Study of Transonic Turbine Cascade Flow

Tibor Kiss,* Joseph A. Schetz,† and Hal L. Moses‡
Virginia Polytechnic Institute and State University, Blacksburg, Virginia 24061

A comprehensive study of the flowfield through a two-dimensional cascade of high-pressure turbine blades is presented. The experimental studies were carried out on a cascade of 11 blades in a blow-down tunnel. The static pressure was measured on the cascade side wall and on the blade surfaces. Total pressure and total temperature measurements were taken upstream of the cascade. Shadowgraph pictures were taken for a study of the trailing-edge shock structure and for the turbulent transition location. A single-plate interferometer technique with a new evaluation method was used for density field measurement. For the numerical studies the full Navier–Stokes equations were solved on a nonperiodic C grid. In the attached boundary layer, the turbulence was modeled by an extension of the Clauser eddy viscosity model developed for compressible flow. In the trailing edge and wake region, the Baldwin–Lomax model was used. Good agreement between the measured and the calculated results was obtained for most aspects of the flowfield.

Nomenclature

C = axial chord
d = image separation
f_{ABf} = number of fringes between A and B, with flow
f_{ABn} = number of fringes between A and B, no flow
M_e = exit Mach number
M_{is} = isentropic Mach number
P = pitch of cascade
p = pressure
p_{tu} = upstream total pressure
x = axial coordinate
y = normal coordinate
λ = wavelength of laser
ρ = density

Introduction

ALTHOUGH considerable progress has been made in the past few years in the numerical simulation of steady two-dimensional transonic turbine cascade flow, in general these numerical results are still not reliable enough. It is especially difficult to match the experimental data in the turbulent and separated flow of the trailing-edge region. Most researchers agree that further improvement is needed in turbulence modeling, grid generation, and convergence acceleration. Since the success of a numerical simulation can be evaluated through comparison with measured data, there is also a strong interest in extending the experimental database for transonic turbine cascade flows. Some measurements, again, are difficult in the most critical trailing-edge region. The present study is a contribution to the efforts to improve the measurement and the numerical simulation of transonic turbine cascade flows. On the experimental side, an interferometer study was performed for density field measurements. The type of interferometer used here was known previously, but it was only used to obtain fringe patterns and not quantitative density field data. For the numerical simulation, a new kind of C type grid was generated, which was specifically developed for transonic turbine cascade flow. Also, a contribution for improved turbulence modeling was attempted; a turbulence model that was developed recently for moderately compressible boundary-layer flows was applied.

Cascade and Facility

The midheight profile of a high-pressure turbine blade in a jet engine was used for the profile of the two-dimensional cascade blades. Since high turning in a wind tunnel is not practical, the profile of the tested blades were modified to have zero inlet angle. This modification had no relevance to the final conclusions, because accurate matching of the specific engine flow was not necessary for the purpose of this work. The tangent of the camber line near the trailing edge was 67 deg. The radius of the trailing edge was 0.02 in., and the axial chord C was 1.5 in. More details about the blade profile can be found elsewhere.[1]

The cascade consisted of 11 blades. The pitch of the cascade, P, was 1.4674 in., and the span was 6 in. On the pressure side, the throat was located right next to the trailing edge. The frame of the cascade was two Plexiglas® plates, called side walls, and the blades were mounted between the side walls with a screw and a pin on both sides. Also, an end block was placed below the first blade and another above the 11th. In this way, 10 blade passages were created and that was enough to provide good periodicity of the flow. In most cases, the flow conditions in the cascade were set by the upstream total pressure. For part of the interferometer studies, however, a tailboard was used to set the exit angle and, thereby, the exit Mach number, since more stable flow could be achieved in this way.

The cascade was placed in the test section of the blow-down type cascade tunnel at Virginia Polytechnic Institute and State University. The upstream total pressure and exit Mach number could be maintained constant within 2% for about 20 s, which determined the maximum time for data acquisition. The tunnel is described in detail in other publications.[1,2]

Pressure Measurements

Figure 1 summarizes the instrumentation used for the pressure measurements. The x axis in the figure was chosen parallel to the inlet flow. The x and y axis both are tangent to blade 4 near the trailing edge. In front of the blades, a single pitot probe (not shown in the figure) was used to measure the upstream total pressure p_{tu}. This pitot probe was mounted on the door of the test section, with its tip outside of the boundary layer. A previous study[2] showed that the total pressure was uniform across the cascade inlet within 1%. For static pressure measurements in the exit area, pressure taps were

---

Presented as Paper 93-3064 at the AIAA 24th Fluid Dynamics Conference, Orlando, FL, July 8–11, 1993; received May 6, 1994; revision received March 21, 1995; accepted for publication March 27, 1995.

*Research Assistant, Department of Aerospace and Ocean Engineering; currently Senior Analysis Engineer, Cummins Engine Co., Fuel Systems Technology, MC 41605, 1460 National Road, Columbus, IN 47201. Member AIAA.

†J. Byron Maupin Professor, Department of Aerospace and Ocean Engineering. Fellow AIAA.

‡Professor, Department of Mechanical Engineering (deceased). Member AIAA.

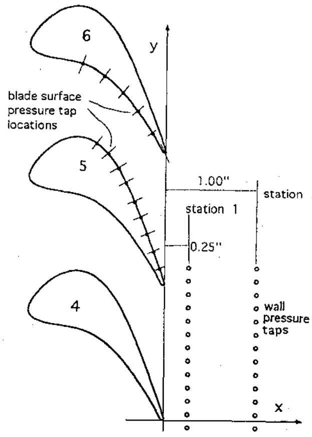

Fig. 1 Cascade and pressure measurement arrangement.

applied on one of the cascade side walls. Two rows of taps were implemented. The first was 0.25 in. behind the trailing edges, and that location will be called station 1. The second row was at 1 in. behind the trailing edges, and that location will be called station 2. Each row consisted of 13 taps. The spacing between the taps within a row was 1/10th of the pitch.

Static pressure measurements were also done on the surface of some specially instrumented blades. Blade 5 (see Fig. 1) was instrumented with 9 taps on the suction side. Blade 6 was instrumented with 5 taps on the pressure side and with 1 tap right on the trailing edge. All of these blade surface static pressure taps were located at midspan. For the pressure measurements, a system with a 32-channel transducer was used, which was scanned so fast that practically simultaneous readings could be obtained on all 32 channels.

The exit Mach number M_e was defined with the average static pressure at station 1, p_e, and the upstream total pressure p_{tu} using the isentropic relationship

$$M_e = \sqrt{\left[\left(\frac{p_{tu}}{p_e}\right)^{\gamma-1/\gamma} - 1\right]\frac{2}{\gamma-1}} \qquad (1)$$

Data were taken for the nominal exit Mach numbers of 0.8, 0.9, 1.0, 1.1, 1.2, and 1.28.

It should be mentioned that for this same cascade flow total pressure loss measurements were also carried out by the addition of a pitot probe traversing across the exit flow. Results of that study can be found in Ref. 1.

Flow Visualization

Shadowgraph Study

For accurate simulation of a cascade flow it is important to determine the turbulent regions in the flowfield. Some turbulence models incorporate provisions to determine the location of transition, however, these methods are not reliable enough for cascade flow. For the present study, the transition locations were determined from shadowgraph pictures. These pictures also allowed for the study of the shock structure. Shadowgraph pictures were taken for the six nominal Mach numbers. As an example, a shadowgraph for exit Mach number 1.2 is shown here in Fig. 2. From the original pictures, the approximate transition location could be detected. For all exit Mach numbers, the transition was found at about $x = -0.25$ in. on the suction side. The flow in our cascade was found to be laminar for the whole pressure side of the blades. Even the trailing-edge separation on the pressure side was found to be laminar. The wake was found to be fully turbulent.

Interferometer Study

For density field measurements, a single-plate interferometer technique[3] was applied. Since this technique is not very well known, it will be described briefly. A single-plate interferometer (see Fig. 3) applies a laser light source. The laser beam passes through a beam expander and a spatial filter. The expanding beam is collimated by a parabolic mirror and is lead through the test section perpendicular to the plane of the flow. The laser beam then hits a glass wedge plate, which has a very low (typically, 10–30 s of arc) wedge angle. Part of the beam reflects from the front surface of the wedge plate, whereas the rest of the light penetrates into the plate and reflects from the back surface. In this way, two overlapping beams are created which cross each other at a slight angle. Although the optical path lengths of the two beams are different, the coherence length of the laser light is long enough to produce a fringe pattern that is dependent on the density field in the test section. Pictures are taken of this fringe pattern focusing on the center of the test section with a second parabolic mirror. It can be seen from Fig. 3 that an object in the test section has two images on the picture. This double image feature is characteristic of the single-plate interferometer.

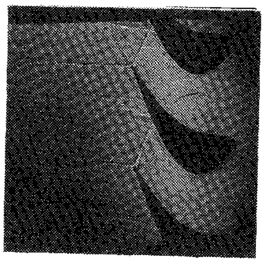

Fig. 2 Shadowgraph for $M_e = 1.2$.

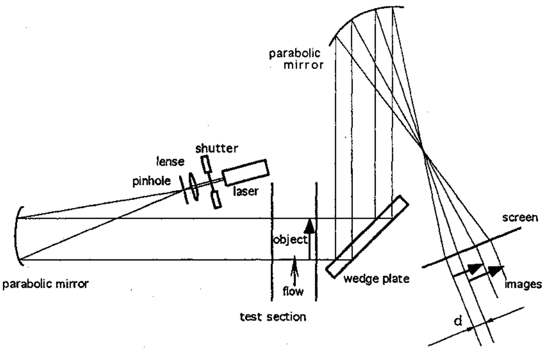

Fig. 3 Schematic of the single-plate interferometer.

The single-plate interferometer has some advantages compared to the Mach–Zehnder interferometer. Because of the long coherence length of the laser, no compensation chamber is needed. Also, since the wedge angle of the plate does not change with the possible vibration of the wind-tunnel environment, there is no need for heavy vibration free mounting of the wedge plate. Furthermore, only a single wedge plate is needed which can be a schlieren quality wind-tunnel window, compared to two beam splitters and two mirrors for the Mach–Zehnder interferometer. A disadvantage is that the picture quality is not quite as good as with the Mach–Zehnder interferometer due to some weak background fringe patterns caused by the laser. Another disadvantage is that the interpretation of the interferograms is more difficult.

In fact, to the best knowledge of the authors, a method to evaluate the density field from a single-plate interferogram has never been published before. Therefore, as part of this project, an evaluation method had to be developed. Details of the derivation can be found in Ref. 4. Here only the final result is presented.

Consider Fig. 4, which depicts the image formation for a certain orientation of the wedge plate (the mirrors are not included for simplicity). If one picks two points, A and B in the interferogram, with the help of the figure, the $A1$, $A2$, $B1$, and $B2$ points can be traced back to the test section of the tunnel. Then, the following relationship can be written between the densities in these points:

$$(\rho_{A1} - \rho_{B1}) - (\rho_{A2} - \rho_{B2}) = (\lambda/K)(f_{ABf} - f_{ABn}) \qquad (2)$$

The K constant is given by[5]

$$K = (Lk)/(n_0\rho_{\text{ref}}) \qquad (3)$$

where L is the width of the test section (span), n_0 is the index of refraction for ambient air, ρ_{ref} is a reference density (1.252 kg/m^3), and $k = 3 \times 10^{-4}$.

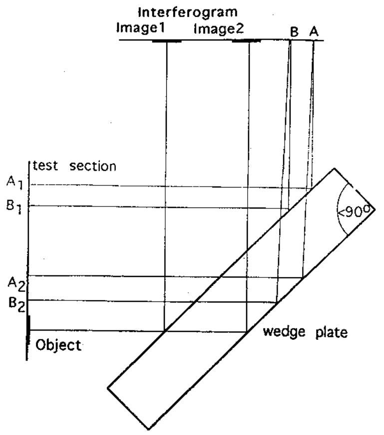

Fig. 4 Image formation for a specific wedge-plate orientation.

Looking at Eq. (2), it is clear that if the absolute value of the density at a given point is to be found with the single-plate interferometer technique, the density has to be known at three other locations. This inherent feature, in general, is not to the advantage of this technique. It can be shown, however, that when the density is known in a band that has a width of the image separation distance *d* then the density can be found anywhere else in the test section.[4]

The single-plate interferograms can be useful for the comparison with numerical results even if there is no region in the flow with known density field. The numerical results can be used to generate corresponding fringes numerically using Eq. (2), and this numerical interferogram can be compared with the real interferogram. In case of agreement, however, it cannot be unequivocally concluded that the calculated density field is accurate. It can be shown that if the numerically obtained density field has a linear error of $b + cx$, the numerical fringes will be exactly the same as the ones obtained with the true density field.[4]

The single-plate interferometer apparatus included a 15-mW helium-neon laser as a light source. The wedge plate was 6 in. in diameter and had a thickness of 7/8 in. The wedge angle of the wedge plate was 15 s of arc. Achieving adequate exposure time was troublesome with a continuous laser. Because of the instabilities in the flowfield, 50 μs or less exposure time was needed. A special shutter[4] had to be built with the use of a Bragg-cell and a photodiode. With this shutter, the exposure time could be set in the nanosecond range. Even with a reduction of the image sizes, however, the low intensity of the laser light did not allow for exposure times less than about 25 μs. For interferometer applications, good quality glass windows were needed. The windows were 2 × 2 in. square pieces with $\lambda/4$ flatness. The windows were placed as far upstream as possible without being too close to the blade support pins. They were embedded in the Plexiglas side walls of the cascade.

Interferograms of the cascade flow were taken with the wedge plate orientation shown in Fig. 4 for all six nominal exit Mach numbers. Since density measurement of appropriate reference regions of the flowfield was not possible, these pictures were not suitable for the evaluation of the density field in any region. A low exit Mach number example will be shown in Fig. 12 where it is compared to an interferogram simulated from the numerical results. Note, that the second image of the trailing edge is outside the edges of the picture.

Absolute density measurement was possible using a cascade of enlarged blades. These blades had the same profile shape as the original ones, however, their axial chord was 5 in. The same 2 × 2 in. windows were used which now covered a region upstream of the trailing-edge shocks, where, outside of the boundary layer, the total pressure could be taken as the upstream total pressure and the total temperature could be taken as the upstream total temperature. Then, with the static pressure which is measurable by wall pressure taps, a reference density field could be obtained in a band of sufficient width.

The interferograms were taken again with the orientation of the wedge plate shown in Fig. 4. For better resolution of the small trailing edge region, the images could not be reduced for higher illumination, therefore, the exposure time had to be increased. The longer exposure time resulted in intolerable blur due to the instabilities in the flow, until the previously mentioned tailboard was implemented. With the tailboard, the flow was turned by the stable surface of the tailboard instead of an unstable free shear layer, and most of the instabilities were eliminated.

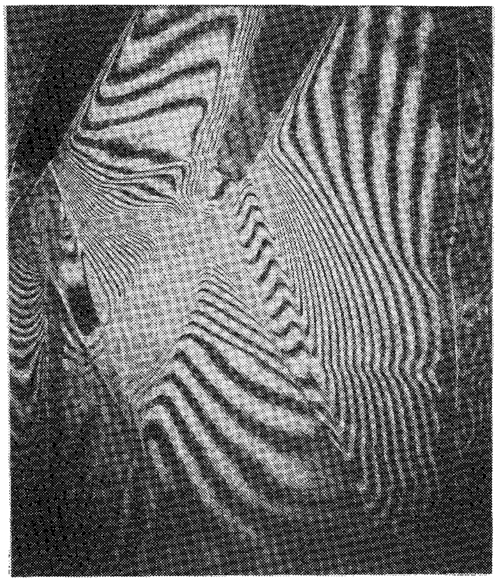

Fig. 5 Interferogram of the trailing-edge region of the enlarged blades, $M_e = 1.2$.

The interferogram of the trailing-edge flow of the large blades for exit Mach number 1.2 can be seen in Fig. 5. In this picture, both images of a single trailing edge can be seen. The density field around the trailing edge was evaluated with the help of the reference density field, and it is in good qualitative agreement with the physics of the flowfield (see Fig. 13). The contour lines show that the density is considerably higher on the pressure side than it is on the suction side. On both the suction and pressure sides, the development of the trailing-edge shocks from the compression waves can be detected. The density rise through these shocks is clearly seen. Also, the expansion wave is clearly shown on the pressure-side trailing-edge lip. Furthermore, the density decrease in the boundary layers on both sides is indicated, as is the density decrease in the wake.

Numerical Studies

The computational fluid dynamics (CFD) code ANSERS[6] was used for the numerical studies. The two-dimensional, cell-centered finite volume formulation of the complete Navier–Stokes equations was solved. The upwind formulation was implemented with Roe's flux difference method. Flux limiting was done with the min-mod method. Spatial discretization of the inviscid terms was carried out on the third order in both coordinate directions. Spatial discretization of the viscous terms were on the second order. The resulting formulation was solved with time relaxation using a spatially split approximate factorization method. Since the goal was to obtain the steady-state solution, the calculation was not time accurate. To accelerate convergence, variable time step was used over the grid cells.

Grid Generation

Because of the blunt leading and trailing edges and because of the high turning of the flow, the generation of a sufficient grid was not trivial. The code was not capable of multiple grid calculations, the grid had to be a single, structured grid.

The structured grids are usually classified into three types: H grids, O grids, and C grids.[7] Depending on the problem, any of these can be the best choice. For wall-bounded or channel flows the H type grid is usually sufficient. For infinite flowfields around airfoils the O type grid is more advantageous. For periodic, cascade flows all three kinds have been used. A good summary of the advantages and disadvantages of the different types of grids as applied to cascade problems is given in a work by Arnoe et al.[8] In the following analysis, some of their conclusions will be incorporated.

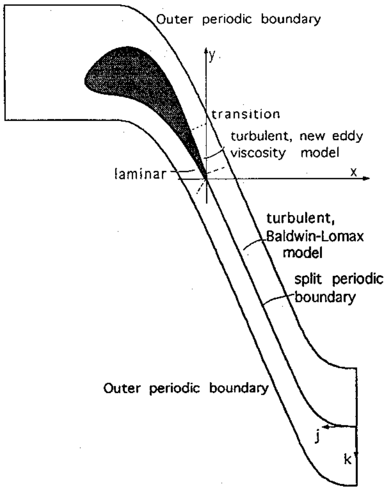

Fig. 6 Computational domain and turbulence modeling choices.

The H grid, which is probably the easiest to generate, has poor resolution of the flowfield near blunt leading and trailing edges. Also, on the leading edge, because of the grid distortion, there is spurious entropy generation that is carried downstream on the blade surface. For an O type grid that problem is avoided but others arise. If the calculations have to be carried out far downstream, then, for sufficient resolution of the wake and trailing shock area, a great number of O grid lines are needed. These grid lines pass through upstream of the blade too, causing a much higher grid density there than would be necessary, thereby wasting computer time. Also, for domains not extending too far in the wake area, a high distortion of the grid cells cannot be avoided. When a single grid extending far downstream is needed, a C type grid is advantageous. The C type grid is like the O type near the leading edge and like the H type near the trailing edge. In this way, there is less spurious entropy addition at the leading edge, and the different domains of the flowfield can be filled up with grid points at the right density. For these reasons, a C type grid was chosen for the calculations described here.

The computational domain extended 1.78 in. downstream in axial direction, so that comparison with the interferometer results could be possible. Also, to avoid complications in the wake turbulence modeling, the domain had to contain the wake for most of the downstream part, which meant the computation domain had to turn with the flow. At the farthest downstream, the upper and lower edges curved back to the horizontal to from a right angle with the outflow boundary. Because of the periodicity of the flow, the upper and lower edges of the domain had to have the same shape and had to be separated in the y direction by one blade pitch. The computational domain selected to meet these criteria can be seen in Fig. 6.

The easiest way to implement periodic boundary conditions is to generate a C grid which is periodic at both periodic boundaries, that is, the mesh points on the upper and lower boundaries are at the same x locations. With a C grid like that, however, a serious skewness of the grid cells cannot be avoided. Therefore, Arnoe et al.[8] proposed a grid which was not periodic on the split periodic boundary. The constraint of grid periodicity, however, can just as well be removed from the outer periodic boundaries, as was also pointed out by the same authors. For the present application, this second arrangement proved to be more advantageous. Because of the relatively higher concentration of grid points near the trailing edge, the grid required clustering on the outer boundaries as well, in order to take up a great number of grid lines coming from the trailing-edge region and thereby to avoid a badly skewed grid. Now, for a grid periodic on the outer boundaries, the center of clustering has to be at the same x location on the lower and upper boundaries. This would have, again, lead to highly skewed grid cells. Also, with a nonperiodic grid on the outer boundaries, grid lines can come from the trailing-edge region and can run parallel with the trailing-edge shocks, thereby extending the trailing-edge clustering to the domain of the flow with the highest gradients. In this way, the trailing-edge shock system will be sharp, facilitating effective comparison with shadowgraph and interferometer pictures.

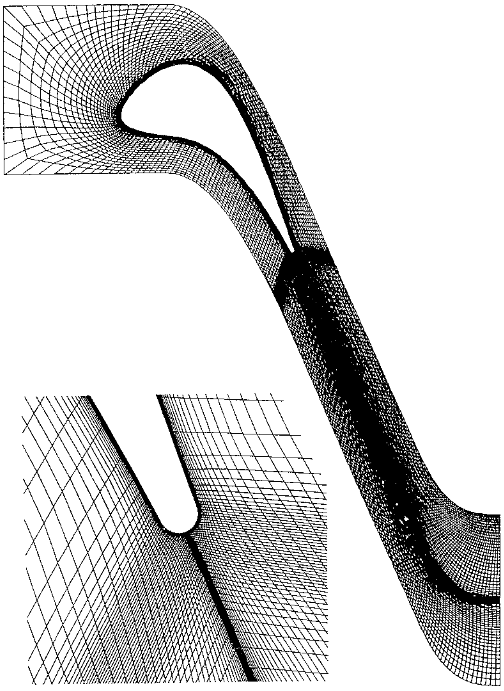

Fig. 7 Nonperiodic 437 × 45 C type grid.

The shear layers had to be sufficiently resolved too. With a strong clustering of the grid points, it was assured that the grid points closest to the blade surface were well inside the laminar sublayer of the turbulent boundary layer. Some clustering was needed also in the wake region in order to sufficiently resolve the wake.

The final grid with the trailing-edge region as an inset can be seen in Fig. 7. The actual size of this grid is 437 × 45, and this size was determined by the available computer power. A reduced 219 × 23 grid was also constructed from this fine grid by removing every other grid line in both grid directions. From this second grid a third 110 × 12 grid was constructed in the same way. The final grid was generated using several codes. A code was written which distributed the grid points on the grid boundaries according to a density function. Then, the code GRAPE[7] was used, which generated a grid with an algorithm based on an elliptic solver. The resulting grid was checked, and the areas which were not satisfactory were identified. Then, the density function was changed accordingly, and the grid points on the boundaries were redistributed. This process continued until a satisfactory grid was obtained. Later, the trailing-edge part of the grid was revised, since a more advanced software, GRIDGEN,[9] became available.

Turbulence Modeling

In the attached suction side boundary layer close to the trailing edge, the local Mach number can be as high as 1.6 for higher exit Mach numbers. Therefore, a turbulence model that was derived for moderately compressible flow is preferable. The curvature of the blades on the suction side is fairly low, and the pressure and edge velocity gradients are not very high compared to the boundary-layer thickness. Such a boundary layer can be calculated with relatively simple algebraic turbulence models just as well as with a more complicated and less time efficient one or two equation models. The well-known Clauser model[10] could be used, except that the original formulation is valid for incompressible boundary-layer flow only. Therefore, a study was conducted which resulted in an extension of the Clauser model to compressible flow,[11] and this model was used for calculating the eddy viscosity in the outer part of the suction side boundary layer. For the viscous sublayer, the Reichardt model was implemented.[10] Since the Baldwin–Lomax model[12] has some advantages over other methods facilitating numerical applications, this model was chosen for the turbulence modeling in the far wake region.

There are no widely used and successful algebraic models which were specifically designed for the trailing-edge flow. However, the

Baldwin–Lomax model has some good features for the use in this region too. First, the Baldwin–Lomax model can be used in separated flows with small separation region, such as the trailing-edge flow. Second, it provides a relatively smooth continuous transition of the length scale of the boundary layer into the length scale of the far wake. Therefore, the Baldwin–Lomax model was used not only in the far wake region but also in the near wake region and over the suction side of the trailing edge.

Boundary Conditions and Convergence

At the exit boundary, the axial velocity was not supersonic. Therefore, the back pressure was specified such that the desired exit Mach number was obtained. For the subsonic inlet boundary, the total pressure and the total temperature were held at the measured values. Also, the y velocity component was taken zero, and the x velocity component was extrapolated. Because of the matching cell faces, for the split periodic boundary the implementation of the periodic boundary condition was trivial. For the outer periodic boundary with the cell faces not aligned, an adequate conservative interpolation had to be used.

Each nominal exit Mach number case was run on all three grid sizes. Not only could the grid convergence be studied this way, but also, by interpolating the result from a coarser grid on finer grid, the total CPU time needed for obtaining a solution on the finer grid was substantially reduced. On each of the three different grids 2–5000 iterations were needed for convergence. The total CPU time to obtain a solution on the finest grid was about 3000 s, running the problem on an IBM 3090 computer. The residual drop, starting from initializing with the inlet conditions, was 3.5 orders of magnitude on the coarsest grid and about 2 orders of magnitude on the finest grid.

Results

In Fig. 8, the predicted contour plot of the Mach number for the $M_e = 1.2$ case is presented. This result shows that the calculation reflected the proper physics of the flow. The locations of the trailing-edge shocks given in the shadowgraph of Fig. 2 are well matched. The velocity vectors in the trailing-edge region nicely show the trailing-edge separation in Fig. 9. The lack of symmetry in the trailing-edge flow is partly due to the fact that on the pressure side the separation is laminar, whereas on the suction side the separation is turbulent.

The static pressure results were converted into isentropic Mach numbers with Eq. (2) using the appropriate static pressure instead of p_e. In Fig. 10, the side-wall isentropic Mach numbers are shown for station 1 for the $M_e = 1.1$ case. Results from all three grid sizes are included. It can be seen that the results from the two finer grids are almost the same, therefore, grid convergence was well approached. Another observation is that the measured isentropic Mach numbers are smeared out to some extent through the shock waves. In the real flowfield on the cascade side walls, boundary layers develop in which close to the wall the Mach number is less than 1.0. Consequently, the shocks of the flowfield cannot extend deep into the boundary layers, and on the wall the sharp pressure drop through a shock cannot be detected. Having lower grid density has a similar effect. The larger grid cells cannot resolve the high-flow gradients, and the sharp drop of static pressure across the shock is smeared out in a similar manner. This is the reason why the solution on the 110×12 grid appears to match the measured data the best.

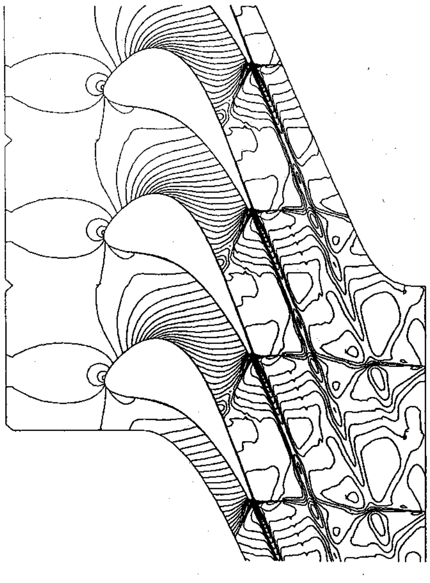

Fig. 8 Predicted Mach number contours for $M_e = 1.2$.

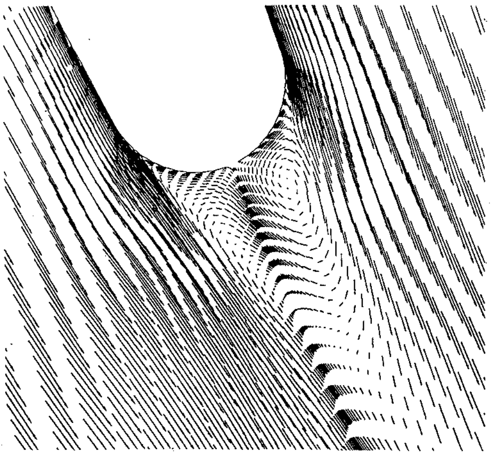

Fig. 9 Predicted velocity vectors near the trailing edge, $M_e = 1.2$.

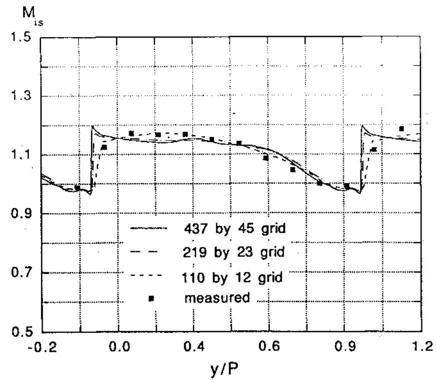

Fig. 10 Comparison of measured and predicted isentropic Mach number profiles at station 1, $M_e = 1.1$.

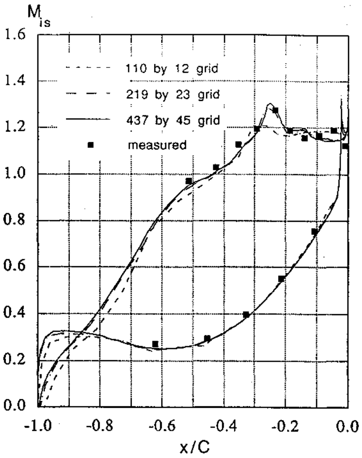

Fig. 11 Comparison of measured and predicted blade surface isentropic Mach numbers, $M_e = 1.1$.

For the blade surface measurements, the isentropic Mach numbers obtained from the measured and calculated pressure data are shown in Fig. 11. Again, the $M_e = 1.1$ case was chosen, and results on all three grid sizes are included to prove grid convergence. The largest

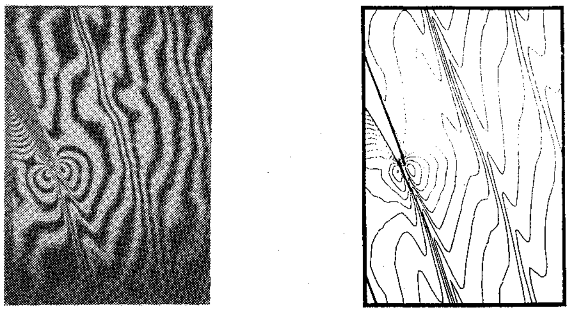

a) Experimental b) Numerical

Fig. 12 Interferograms for the original blades, $M_e = 0.8$.

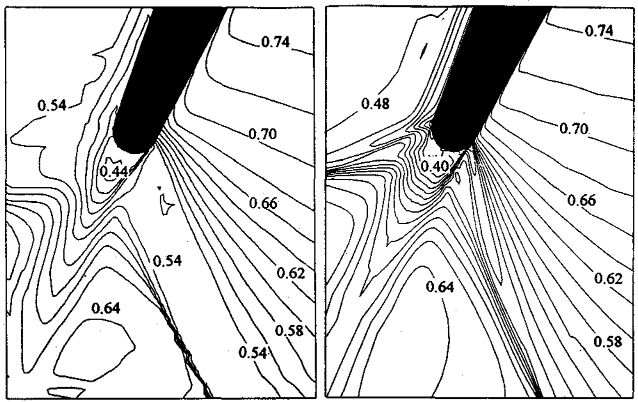

a) From interferogram b) From calculations

Fig. 13 Density fields around the trailing edge of the enlarged blade, $M_e = 1.2$.

deviations from the measured results were obtained on the suction side, behind the impinging trailing-edge shock and on the trailing edge. The predictions, however, are fairly good even in those regions.

The numerical fringe pattern along with the experimental interferogram for the cascade of the original blades with $M_e = 0.8$ flow are presented in Fig. 12. It can be seen that for this low-Mach-number case the agreement is quite good. Unfortunately, for higher Mach numbers, the instabilities in the flowfield resulted in unclear pictures, and the comparison between the numerical and experimental fringes was difficult.

For the comparison with the large blade trailing-edge interferogram, a calculation of the large blade cascade flow was also carried out. The differences compared to the calculation with the original blade included a different Reynolds number, different upstream conditions, and a different turbulent transition location. The trailing-edge density contours are shown in Fig. 13. It can be seen that the density results by the two methods are in good agreement on the pressure side; however, on the suction side and near the trailing edge there is some disagreement. The reasons for this disagreement can be due to some three dimensionality of the flow and/or the deficiencies of the turbulence modeling.

Conclusions

A comprehensive study of a flow through a transonic turbine cascade has been presented. The experimental studies included conventional pressure measurements, a shadowgraph technique and a not well-known interferometer technique. As a result of the shadowgraph study, the location of turbulent transition was determined with sufficient accuracy. It should be noted that this method could be used on different blade profiles for the improvement of turbulent transition prediction methods.

The interferometer studies were carried out with a single-plate interferometer technique. The assembly and the application of the single-plate interferometer proved to be easier than that of a Mach–Zehnder interferometer, the evaluation of the pictures was more difficult. The evaluation method worked out by the authors was briefly explained, and the method was applied. With the new method, physically realistic density field was obtained in the trailing-edge region of a large blade. Also, based on the evaluation method, a fringe pattern was generated from the numerically obtained density field. This fringe pattern matched the interferogram's fringe pattern quite well outside of the shear flow regions, that is, in the region where the CFD results are generally reliable. These results provided a first verification of the evaluation method. The interferometer measurement technique can certainly be improved beyond its capacity in this first application, and it may serve as a simple and valuable experimental tool in the future. On the one hand, it can serve to help verify the calculated mean flow results. On the other hand, it can be used for nonintrusive density measurements in restricted, highly viscous regions of the flowfield, such as the trailing-edge region or the boundary layer.

The numerical results matched the experimentally obtained data quite well for most aspects of the flow as a whole. Best agreement was obtained for the isentropic Mach numbers over the blade surface and in the exit region and for the density field outside of the shear layers.

In the shear layers the matching was not quite as good. The calculated wakes were thinner and stronger, as follows from the comparison of the experimental and numerical interferograms. Because of our higher confidence in the boundary-layer and far-wake turbulence models, it was implied that the mixing in the near-wake region was stronger than the Baldwin–Lomax turbulence model predicted. An explanation could be that instead of the smooth transition of turbulent length scale between the boundary layer and the far-wake region, a sudden increase in length scale occurs right behind the trailing edge. It can be argued that the size of the turbulent eddies is suddenly not restricted any more by the presence of the blade surface. More work is needed either to prove this hypothesis or to identify some other processes that could be the cause for the apparent higher degree of mixing in this region.

The calculated density field in the large blade trailing-edge region was reasonably close to the measured result obtained from the interferogram, especially if we consider the complexity of the flowfield. Differences were possibly due to inaccuracies in both the calculation and the measurement. The trailing-edge region seems to remain the part of the flowfield that is the most difficult to measure and predict.

References

[1] Bertsch, R., "An Experimental Examination of the Influence of Trailing-Edge Coolant Ejection on Blade Losses in Transonic Turbine Cascades," M.S. Thesis, Dept. of Mechanical Engineering, Virginia Polytechnic Inst. and State Univ., Blacksburg, VA, Dec. 1990.

[2] Zaccaria, M. A., "Development of a Transonic Cascade Facility," M.S. Thesis, Dept. of Mechanical Engineering, Virginia Polytechnic Inst. and State Univ., Blacksburg, VA, 1988

[3] Sedney, R., Rowe, R., Bush, C., and Voelker, L., "Conventional Flow Visualization Using Laser Light Source," AIAA Paper 66-127, Jan. 1966.

[4] Kiss, T., "Experimental and Numerical Investigation of Transonic Turbine Cascade Flow," Ph.D. Dissertation, Dept. of Aerospace and Ocean Engineering, Virginia Polytechnic Inst. and State Univ., Blacksburg, VA, Dec. 1992.

[5] Weinberg, F. J., *Optics of Flames*, Butterworths, London, 1966.

[6] Taylor, A. C., III, "Convergence Acceleration of Upwind Relaxation Methods for the Navier–Stokes Equations," Ph.D. Dissertation, Dept. of Mechanical Engineering, Virginia Polytechnic Inst. and State Univ., Blacksburg, VA, 1989.

[7] Sorenson, R. L., "A Computer Program to Generate Two-Dimensional Grids about Airfoils and Other Shapes by the Use of Poisson's Equation," NASA TM 81198.

[8] Arnoe, A., Liou, M.-S., and Povinelli, L. A., "Transonic Cascade Flow Calculations Using Non-Periodic C-Type Grids," Computational Fluid Dynamics Symposium on Aeropropulsion Conf., April 1990 (preprint from CP-3078).

[9] Steinbrenner, J. P., Chawner, J. R., and Fouts, C. L., "The GRIDGEN3D Multiple Block Grid Generation System," U.S. Air Force Wright Research and Development Center, WRDC-TR-90-3022, Vol.1–2, July 1990.

[10] Schetz, J. A., *Boundary Layer Analysis*, Prentice–Hall, Englewood Cliffs, NJ, 1993.

[11] Kiss, T., and Schetz, J. A., "Rational Extension of the Clauser Eddy Viscosity Model to Compressible Boundary-Layer Flow," *AIAA Journal*, Vol. 31, No. 6, 1993, pp. 1007–1013.

[12] Baldwin, B. S., and Lomax, H., "Thin Layer Approximation and Algebraic Model for Separated Turbulent Flows," AIAA Paper 78-257, 1978.